

# THE CLEAN SKY ‘CARD’ PROJECT: WIND TUNNEL MEASUREMENTS OF A MODEL HELICOPTER ROTOR AND FUSELAGE DRAG

R.B. Green, M. Giuni, University of Glasgow, UK

*and*

J. Červinka, D. Zacho

Výzkumný a Zkušební Letecký Ústav (VZLÚ), Prague, Czech Republic

*and*

P. Austin, S. Smith, Aircraft Research Association, Bedford, UK

*and*

D. Desvigne, D. Alfano, Airbus Helicopters S.A.S., Marignane, France

## ABSTRACT

Results of a wind tunnel test campaign to assess technologies for improvement of helicopter fuselage and rotor system drag are described in this paper. The work done was part of the EU funded Clean Sky CARD project (Contribution to Analysis of Rotor-hub Drag reduction). Wind tunnel tests of an accurate 1/4 scale, Airbus Helicopters H155 were performed in a variety of advance ratios, pitch angles and side-slip angles to simulate cruise and approach conditions. 1/3rd of the rotor diameter was represented in the model, and the rotor was otherwise rigid and un-actuated (fixed blade pitch around the azimuth). Rotor system forces and moments were measured independently of the fuselage forces and moments, thus allowing the various contributions to the total drag to be evaluated. The paper describes elements of the model design and data analysis for drag and power evaluation, and presents sample results.

## NOMENCLATURE

$c$	blade chord
$C_D S$	dimensional drag coefficient, $C_D S = \frac{F_D}{q}$
$F$	force
$F_D$	drag
$F_L$	lift
$F_{ma}$	rotor/ beanie in-plane force resolved in model axis direction
$F_p$	rotor/ beanie in-plane force resolved in lateral direction to model
$F_x, F_y, F_z$	load cell component forces
$\tilde{F}_z$	adjusted $F_z$ for rotating rotor drag calculation
$q$	wind tunnel dynamic pressure
$S$	load cell sensitivity
$U_\infty$	wind tunnel speed
$V$	load cell voltage
$V_d$	load cell dynamic offset
$V_{\text{drift}}$	load cell drift
$V_o$	load cell systematic offset
$V_{\text{off}}$	load cell offset voltage
$V_{qs}$	load cell quasi-static offset
$W$	weight
$x_{\text{rotor}}, y_{\text{rotor}}, z_{\text{rotor}}$	rotor coordinate system
$x_{\text{WT}}, y_{\text{WT}}, z_{\text{WT}}$	wind tunnel coordinate system
$\alpha$	model angle of attack
$\beta$	model yaw angle
$\epsilon$	rotor shaft tilt angle
$\mu$	advance ratio
$\psi$	rotor azimuth
$\theta$	blade pitch angle

# 1 INTRODUCTION

It is well known that helicopters have high aerodynamic drag compared to fixed wing aircraft. While the fuselage and rotor blades *in isolation* can be designed to be as aerodynamically efficient as possible, the complex aerodynamic environment of the rotor system and associated interactions can lead to a higher overall drag than otherwise expected. High drag compromises the endurance of the helicopter, and presents an additional operational expense. Furthermore combustion emissions need to be reduced, and high drag presents a challenge to this goal. Prouty<sup>1</sup> provides a typical drag breakdown of a helicopter; the rotor hub and shaft were reckoned to account for 35% of parasitic drag, while rotor-fuselage interference effects accounted for another 7%. That article was first presented almost 30 years ago, but the analysis is still representative (Desvigne and Alfano<sup>2</sup>). Any attempt to reduce the drag of the helicopter must address the aerodynamic environment of the rotor hub and the surrounding fuselage area.

For an efficient overview of overall helicopter drag the reader is referred to the texts by Johnson<sup>3</sup> and Leishman.<sup>4</sup> It has been recognised clearly for a long time that interactional aerodynamics are significant for the helicopter, and it is well known that this is a significant source of vibration and noise. Sheridan and Smith<sup>5</sup> introduced interactional aerodynamics as a “new challenge” for helicopter technology in a paper published 35 years ago, and the fundamentals of its relevance to helicopter drag are usefully assessed in a paper by Roesch and Dequin.<sup>6</sup> Individual major airframe aerodynamic components such as blades and the fuselage may be designed well for aerodynamic performance, but the pylon fairing is little more than a faired bluff-body, and pitch links, lag dampers, blade sleeves and other parts located in the rotor hub generate significant amounts of separated flow. Trailing vortices are also formed at the blade roots. Drag analysis and reduction for the helicopter is therefore a tremendously difficult task compared to that for a fixed wing aircraft. Computational Fluid Dynamics has the advantage that the drag contributions due to each component can be resolved,<sup>2</sup> and this can assist with an interpretation of the physical significance of the mechanisms at play (Shenoy *et al.*<sup>7</sup>). Active flow control is a technology that may be useful in tackling the various challenges caused by flow separation and wake interactions, and this is gaining some interest; a useful review is provided by a useful review of this is provided by Le Pape,<sup>8</sup> and see for example Potsdam and LePape<sup>9</sup> and Schaeffler *et al.*<sup>10</sup>

The need to reduce helicopter drag is clear and is widely recognised, and research projects to investigate helicopter drag reduction under the EU Clean Sky Green Rotorcraft Research Programme reflect this.

This paper presents results from the CARD project (Contribution to Analysis of Rotor hub Drag reduction). While analysis of the helicopter aerodynamics is a significant challenge for computational fluid dynamics, a wind tunnel experiment to validate designs and provide research data must be able to separate out the various contributions to the drag due to the rotor components and the fuselage. Thus the goal of the CARD project was to perform wind tunnel tests of a representative helicopter configuration to obtain rotor system and fuselage drag data. With the aim of investigation of drag reduction, several innovative hub fairings were investigated. The paper focusses on the details of the experimental design and data analysis, and sample results are shown together with an analysis of overall drag reduction.

## 2 EXPERIMENTAL DETAILS

Tests of a specially designed, 1/4 scale, Airbus Helicopters H155 were performed in the 3m diameter, open-return, low speed wind tunnel at VZLÚ in Prague, Czech Republic. The majority of the testing was performed in September 2013. This wind tunnel is capable of a maximum test speed of  $60\text{ms}^{-1}$ , but tests were run at speeds subject to the loading limits of the sensors, the rotor rotational speed and required advance ratio. A photograph of the model installed in the wind tunnel is shown in figure 1. There is no fenestron and empennage, and one-third of the rotor diameter was represented. The model was mounted on a vertical sting, and the model positioning system allowed model pitch and yaw to be varied. The rotor system, set at a shaft tilt angle of  $\epsilon = -4^\circ$  (tilted forwards), was a rigid, five blade, unarticulated hub. Short, stub blade roots at 1/4 scale chord and made of autoclave cured carbon fibre were installed on the model such that one-third of the rotor diameter was represented (thus test model rotor diameter was 1m). This reduced diameter has the advantage that the complex aeromechanics effects of a full rotor system are diminished, which would otherwise have led to a prohibitively complex and expensive rotor system design; the key feature was that the interaction effects in the blade hub region were represented. Non-functioning pitch links were installed on the hub, but aerodynamic representation of the lead-lag dampers was not included. The blade roots were fixed to blade sleeves attached to the rotor mast. Blade collective was fixed during a test, but could be set to discrete angles between tests. The blade sleeves comprised flanges and webs to form a realistic but rigid aerodynamic representation of the blade mounting flexures on the H155, and figure 2 shows the blade stub roots and sleeves. Two different sets of blade sleeve fairings were fitted as part of the investigation of drag behaviour. Partial fairings covered the upper and lower flanges of the blade sleeve

only, while full fairings covered the sleeve webs and flanges. Both fairing shapes presented an improved aerodynamic profile to the flow and were designed for improved drag performance. Figure 3 emphasises the rotor system beanie, and three different beanies were fitted to the rotor. The baseline beanie was an accurate, scale model of the H155 beanie, while the modified beanies featured different profiles. Power for the rotor was supplied by a compact, electric motor drive. While the individual components were manufactured to a high tolerance, the assembled rotating system was checked for dynamic balancing. Provision for installation of balance weights was made in the rotor blade stubs. Precision measurement of the rotor system in spin up tests on a dynamic balancing rig was performed; vibration level of G1.0 was requested in the design specification, but a vibration level of G0.35 was obtained during balance testing, so no balance weights were required. The fuselage was an accurate, 1/4 scale mock up of the H155 made out of carbon fibre. Engine intakes were closed, representative exhaust plumes were fitted, and, while the fenestron and tail empennage were not fitted, the tailboom included the fenestron shaft tunnel. The surface finish of the model was aerodynamically smooth, and there were no panel or window seams or any other surface excrescences. Two different designs of the aft portion of the pylon were fitted to the model, and figure 4 shows the baseline pylon fairing that tested for the effect on drag; the other pylon tested featured a unique surface profile.

The model was designed to allow the rotor system forces to be measured independently of the fuselage forces, and figure 5 shows a schematic diagram of the notional layout of the loads sensors and wind tunnel model. The fuselage was attached onto the live side of the VZLÚ sting balance, while the rotor system was attached to the ground side of the sting balance. Two co-axially arranged load cells, coincident with the rotor axis and rotating with the rotor shaft, were used to support the rotor and beanie independently, with the ground side of each load cell attached to a common point on the rotor shaft, thus allowing rotor and beanie loads to be separated and measured. Each load cell was an Advanced Mechanical Technology Incorporated (AMTI) model FS6 six component force and moment sensor with standard loads ranges; the axial force rating for the rotor load cell was 2.2kN, while the beanie load cell axial force rating was 440N. Data from the rotating system (rotor and beanie load cells) were fed out of the rotor system via a 32 channel a slip ring set, and the slip rings also carried the load cell excitation voltages. AMTI Gen5 amplifiers were used with the load cells, and excitation voltages and channel gains were adjusted to maximise resolution for each channel, dependent upon force and moment levels anticipated during the tests. Factory calibrations were

used for the load cells. The VZLÚ sting balance measured all three orthogonal forces and moments. While the wind tunnel balance axis system moved with the model pitch and yaw attitudes, the rotor and beanie load axes also rotated with the rotor.

Other sensors mounted in the model included two three-axis accelerometers, one positioned close to the rotor and beanie load cells, and the other close to the end of the sting support. Two platinum resistance thermometers were used to monitor motor body temperature and model internal temperature. Data acquisition for all the model sensors, but excluding the wind tunnel sting balance, was performed using a D-tAcq solutions ACQ-164 model, 24 bit, +/-10V range, 64 channel, simultaneous data recorder capable of sampling up to 128kHz per channel. Communication between the host PC and the data acquisition device was through a TCP/IP interface programmed using National Instruments Labview. Limited data analysis was done on-line for load cell limit, vibration and temperature level monitoring, with detailed data analysis performed off-line using matlab scripts. The wind tunnel sting balance data recording, model attitude setting and wind tunnel control were all handled by the VZLÚ wind tunnel control and acquisition systems.

## 2.1 Experimental Methodology

Measurements were taken for a range of test conditions. Advance ratios were based upon the full rotor diameter, and not on the 1/3rd reduced diameter of the model, and table 1 shows the notional aerodynamic test conditions. The blade collective was usually  $\theta = 8^\circ$ , but selected tests at other blade collective angles were performed (limitation due to time constraint). Fixed and rotating rotor tests were also performed. Tests were done with the various blade sleeve fairings, beanie and pylon fairing modifications fitted. The sampling rate for the rotor tests was set to 8kHz per channel, 10s worth of data were recorded during wind-on runs (over 100 rotor revolutions). The sampling rate provides over 700 samples per revolution, and while it is more than required it was the lowest sampling rate of the data acquisition system.

The aim of the experiments was to determine aerodynamic drag of the fuselage and rotor system. The load  $F$  is derived from the sensor voltage  $V$  using the relationship

$$F = \frac{V - V_{\text{off}}}{S}, \quad (1)$$

where  $V_{\text{off}}$  is the sensor offset and  $S$  is the sensitivity. Load cells and sting balances suffer from offset drift, and any testing procedure must mitigate against this. The offset is the sum of a signal component  $V_0$  due to the installation and any systematic effects due to the system design, and a drift,  $V_{\text{drift}}$ . To account for any

drift, offsets are usually recorded just before and just after a test, and some systems allow for the drift to be nulled. Of concern here is the signal  $V_o$  for the rotating load cells for rotor system loads measurement. Figure 6 shows a schematic diagram of the rotor system load cell loads with the rotor axis at an arbitrary angle  $\alpha$  from the vertical and with the rotor at an arbitrary azimuth angle  $\psi$ . The load cell forces  $F_x$  and  $F_y$  are in the rotor disc plane, and the load cell axial force  $F_z$  is normal to the disc plane. The rotor centre of gravity position is offset arbitrarily by a distance from the electrical centre of the load cell, but the weight  $W$  always acts vertically downwards. As the rotor rotates the c.g. position rotates about the load cell axis and the in-plane forces  $F_x$  and  $F_y$  change orientation also. While the component of the system weight  $W$  acting in the rotor disc plane remains constant, the component of this force in the  $F_x$  and  $F_y$  directions changes, which causes a change of offset. Thus the rotating load cells have a weight dependent offset that varies as a function of the rotor azimuth angle, and this is referred to as the quasi-static offset  $V_{qs}$ . Furthermore when the rotor is spinning at high speed, the centrifugal load due to displacement of the system c.g. from the rotation axis causes an additional dynamic offset  $V_d$ , and this depends upon the degree of out-of-balance of the rotor system. The dynamic offset is fundamentally a function of the rotational speed as the system c.g. and load cell rotate in exact phase. Thus the signal  $V_o$  for the rotating load cells is given as

$$V_o(\psi) = V_{qs}(\psi) + V_d(\psi). \quad (2)$$

The test procedure had to account for these offsets, and steps were taken to evaluate  $V_{qs}(\psi)$  and  $V_d(\psi)$ . The contribution of the quasi-static offset was evaluated as follows:

1. Wind tunnel off.
2. Set model to required pitch and yaw angle.
3. Zero (null) the load cell amplifier to remove the drift offset (sets  $V_{\text{drift}}$  to a notional zero).
4. Start rotor rotating at a low speed of 60 RPM and sample load cell voltages for at least one rotor revolution, this is the pre-test quasi-static offset  $V_{qs}(\psi)$ .
5. Set wind tunnel and rotor to required test speeds.
6. Record test data  $V(\psi)$ .
7. Turn wind tunnel off and allow rotor to slow down to the low speed of 60 RPM.
8. Sample load cell voltages for at least one rotor revolution, this is the post-test quasi-static offset  $V_{qs}(\psi)$ .

9. Stop rotor, set the model to a different pitch and yaw angle, and repeat above test sequence.

Steps 4 and 8 are for the evaluation of the quasi-static offset  $V_{qs}(\psi)$ , and  $V_{qs}(\psi)$  was recorded twice to account for load cell drift during the actual test measurement. The procedure below was used to determine the dynamic offset:

1. Set rotor collective to zero, and install required rotor sleeve fairings and beanie.
2. Wind tunnel off.
3. Set model to required angle of attack.
4. Zero the load cell amplifier to remove drift offset (sets  $V_{\text{drift}}$  to a notional zero).
5. Start rotor rotating at a low speed of 60 RPM and sample load cell voltages for at least one rotor revolution, this is the pre-test quasi-static offset  $V_{qs}(\psi)$ .
6. Set rotor to required test speed, and record test data  $V(\psi)$ .
7. Slow rotor down to 60RPM, and sample load cell voltages for at least one rotor revolution, this is the post-test quasi-static offset  $V_{qs}(\psi)$ .
8. Repeat from step 4 and run at progressively higher rotational speeds.
9. Repeat from step 2 for different angle of attack.
10. Repeat from step 1 for different configuration.

Thus quasi-static offset data were available for before and after each test allowing drift to be accounted for, and dynamic offset data were available for each configuration. Rotating load cell load variation  $F(\psi)$  is then determined as

$$F(\psi) = \frac{V(\psi) - (V_{qs}(\psi) + V_d(\psi) + V_{\text{drift}})}{S}. \quad (3)$$

In practice, and to avoid accumulation of large amounts of sensor drift, the rotating load cell quasi-static offset recording procedure meant that the data for the fuselage sting balance and rotating load cells were recorded during separate runs. For fuselage loads measurement, wind off and rotor off fuselage load data were recorded for a pitch or yaw angle range, the wind tunnel and rotor were set to the required speed, and the fuselage loads were then measured over the pitch or yaw angle range with the wind tunnel and rotor system running. The procedure was repeated after the test with the wind tunnel and rotor stopped to account for sting balance drift.

## 2.2 Data Analysis

Wind tunnel sting balance and rotor system load cell signals were processed independently. Axis transformations were used to convert from model axis system (defined by the model axis) to aerodynamic axis system (defined by the free stream speed  $U_\infty$ ). For the fuselage data this is relatively straightforward, but analysis of the rotating load cell signals required much more attention. Figures 7 and 8 show diagrams of the rotor axis, wind tunnel axis, model incidence and yaw angles  $\alpha$  and  $\beta$ , and load cell  $F_x$ ,  $F_y$  and  $F_z$  and model forces  $F_{ma}$  and  $F_p$  resolved in the fuselage axis and lateral directions respectively. The rotor azimuth angle  $\psi$  is defined with the reference blade pointing directly aft. The rotor in-plane forces  $F_x$  and  $F_y$  may be resolved into model axis components

$$F_{ma} = F_x \cos \psi + F_y \sin \psi,$$

and

$$F_p = -F_x \sin \psi + F_y \cos \psi.$$

The model axial force  $F_{ma}$  has to be resolved onto the horizontal plane (containing  $U_\infty$ ). The rotor mast is tilted forwards by an angle  $\epsilon$  (a negative value using the conventional notation), so the component of the model axial force acting in the horizontal plane is  $F_{ma} \cos(\alpha + \epsilon)$ . The lateral force  $F_p$  is already in the horizontal plane as its direction is parallel to the model pitch axis. A component of rotor axial force  $F_z$  acts in the horizontal plane due to the pitch angle  $\alpha$  and mast tilt angle  $\epsilon$ , equal to  $F_z \sin(\alpha + \epsilon)$ . All these three force components then have to be resolved into the flow direction  $U_\infty$  due to the sideslip angle  $\beta$ , and therefore the drag force from the rotor or beanie load cell is given by

$$F_D = F_{ma} \cos(\alpha + \epsilon) \cos \beta - F_p \sin \beta + F_z \sin(\alpha + \epsilon) \cos \beta. \quad (4)$$

Use of equation 4 above for the non-rotating rotor is unambiguous, but it requires careful consideration for application to the rotating rotor, however, because when the rotor axis is off vertical, a component of the rotor axial  $F_z$  force acts as forward thrust. Of course the contribution of  $F_z$  to the drag cannot be separated from the contribution to the thrust. Hence inclusion of the load cell  $F_z$  in the rotor drag for the rotating rotor is not straightforward. The rotor resultant is assumed to be a constant in the range of angles of attack investigated in this work, typically  $[-10^\circ, +6^\circ]$ . Indeed, the local angle of attack as seen by the rotor is driven geometrically by the rising angle of the front cowlings, which has been revealed to entail locally always the same flow inflection, provided the boundary layer remains attached. Consequently, the  $F_z$  value measured along the  $z_{\text{rotor}}$  direction for an angle of attack of  $-\epsilon$

was removed from that measured for a given angle of attack  $\alpha$ , such that for the rotating rotor

$$\tilde{F}_z(\alpha) = F_z(\alpha) - F_z(-\epsilon), \quad (5)$$

and then the drag force for the rotating rotor is evaluated from

$$F_D = F_{ma} \cos(\alpha + \epsilon) \cos \beta - F_p \sin \beta + \tilde{F}_z \sin(\alpha + \epsilon) \cos \beta. \quad (6)$$

Rotor lift force is evaluated by axis transformation into the vertical direction, and

$$F_L = -F_{ma} \sin(\alpha + \epsilon) + F_z \cos(\alpha + \epsilon). \quad (7)$$

Signals were pre-processed before loads were calculated. Digital filtering was performed by Fast Fourier Transform, amplitudes above a frequency threshold were nulled, and the signal was then reconstructed. The load cells rotate with the rotor, so presentation of the load cell force data as a time sequence has little meaning. Instead pre-processed voltage data were interpolated onto discrete azimuthal positions around the rotor revolution (typical resolution was  $1^\circ$ ), quasi-static and dynamic offsets were removed and loads calculated at each discrete point, and then the mean and root-mean-square loads statistics at each azimuthal point were evaluated.

## 3 RESULTS AND DISCUSSION

This section will present data to establish the validity of the testing methodology, and provide outline results of the aerodynamics. For the specific rotor system loads measurements, the rotor and beanie load cells are referred to as ‘rotor’ and ‘beanie’ respectively. All data presented are fully processed with quasi-static and dynamic offsets removed appropriately. Rotating rotor aerodynamic test data were filtered at  $20 \times$  the rotor speed. Dimensional quantities are presented in cases where the azimuthal variations are to be considered and are not intended for comparison with other data. A wind tunnel correction of  $-0.58^\circ$  has to be added to the targeted model angle of incidence.

### 3.1 Offset Measurement

Figure 9 shows a typical quasi-static and dynamic offset for the rotor load cell  $F_x$  force taken for a test at zero model pitch angle. Frame (a) shows that the offset drift between the pre- and post- test offset measurements is negligible, and this is a typical result. The peak-to-peak amplitude is around 16N, and the mean is non-zero; as the rotor shaft angle approaches vertical the peak-to-peak amplitude falls and the mean tends to zero. Results of a dynamic offset measurement are

shown in frame (b) of figure 9. The quasi-static offset for this test is the same one as shown in frame (a). The dynamic offset is essentially a high mean value with a small fluctuation. These results show that the quasi-static and dynamic offsets are significant, and their correct removal from the test signal is important.

## 3.2 Rotor System Loads

It is useful to consider the rotor system forces prior to a discussion of the drag.  $F_x$  and  $F_y$  forces change their orientation with respect to the model fuselage axis due to the rotor rotation, and for the current purposes it is useful to consider the model axis force  $F_{ma}$  described earlier. This force always points in the same direction towards the end of the tail boom, and it is of course a significant component of the drag when resolved in the drag force direction. Figure 10 shows the individual contributions to the force  $F_{ma}$  due to the rotor and the beanie for a rotating rotor test at targeted model incidence  $4^\circ$  where the rotor shaft is almost vertical, therefore the force  $F_{ma}$  is equivalent to the drag in the case shown. Blade collective is  $8^\circ$ . The forces are highly unsteady, with the rotor showing ten major peaks per revolution and the beanie five major peaks, corresponding to a factor of two and one of the blade passing frequency respectively. For the rotor this will be due to a wake frequency effect in addition to the blade profile drag. The beanie does have minor detail in its shape corresponding to the number of blades, and the beanie  $F_{ma}$  force peaks almost coincide with alternate rotor  $F_{ma}$  peaks. It may be that the beanie force fluctuation is due to a rotor wake passing frequency. Rotor system  $F_z$  force plotted as a function of azimuth is shown in figure 11 for the same test case. Both rotor and beanie show a remarkable five-per-rev signal, but the beanie  $F_z$  data are modulated with harmonics. The rotor  $F_z$  peak-to-peak amplitude is very large, with minimum force around 0N, but note that there is no cyclic variation of blade pitch. The rotor and major beanie  $F_z$  fluctuations are in phase, and the modulations to the beanie  $F_z$  are possibly due to a wake interaction effect. The load cells also provide the torque, and hence the component power can be evaluated, and figure 12 shows the rotor power for the case under discussion. The average rotor power is 792W, but the average beanie power is negligible and it is not shown. Rotor power varies around the azimuth, and the peak-to-peak variations are about 10% of the mean. There is a strong five-per-rev signal with modulation at higher frequency, indicating an effect owing to tip vortices trailed by the truncated blades.

## 3.3 Drag Forces

### 3.3.1 Fuselage Drag

Fuselage drag is obtained from an axis transformation into the aerodynamic reference frame of all the three model axis forces measured by the sting balance. Figure 13 shows normalised fuselage drag as a function of model angle of incidence at zero yaw angle. A quadratic curve fit is shown to help with the noise on the data, and the results have been normalised by the minimum curve fit drag. From the initial high drag at large nose down attitude, the drag reduces as pitch angle increases, and drag then begins to increase again at a moderate positive incidence.

### 3.3.2 Rotor System Drag

Drag was calculated using the procedure outlined in section 2.2. Data have been normalised with respect to a conveniently chosen value. Normalised drag results for the rotor and beanie for a rotor fixed case are shown in figure 14. The plots are at different blade collective and fixed rotor azimuth. Rotor drag is higher with increased rotor collective, and drag falls as model pitch angle increases. Beanie drag values show no consistent trend with blade collective or azimuth position, and while drag remains fairly constant at nose down model pitch, it increases sharply as model pitch increases for positive  $\alpha$ . The rotor drag at  $\psi = 36^\circ$  is slightly lower than for  $\psi = 0^\circ$ , and differences would be expected due to the slightly different arrangement of the blades in the flow. Rotating rotor system lift and drag are shown in figure 15, and are plotted as a function of model angle of attack. Separate rotor and beanie data are shown, and the values are normalised by their respective values at the targeted model incidence  $\alpha = -10^\circ$ . The rotor configuration is the same as for the fuselage data shown in figure 13, but is different to the non-rotating case shown in figure 14. As  $\alpha$  rises, drag falls and lift increases for both the rotor and the beanie. The rate of drag decrease is similar for both rotor and beanie, but lift increase for the beanie is small compared to the rotor. Figure 16 shows the rotating system power plotted with angle of attack. This increases, and note that the beanie power requirement is negligible so it is not shown separately. While power increases as  $\alpha$  increases, figure 15 shows that rotor system drag and lift decrease and increase respectively. Finally figure 17 shows details of the total drag, which includes the fuselage drag from figure 13. The total drag plotted is normalised with the total drag at targeted model incidence  $\alpha = -10^\circ$ , and total drag decreases as  $\alpha$  rises. The drag contributions are expressed as a fraction of the total at each angle of attack, hence they add up to one. Fuselage contribution increases slightly over the angle of attack range and has an average value of 37.8%. Rotor contribu-

tion falls slightly as  $\alpha$  rises, and has an average value of 56.5%, and the beanie accounts for the remaining 5.7%. The contribution to the total drag of the rotor head is more than the expected value of around 35% to 40%, and this may be because of the presence of a significant portion of the rotor blade on the model.

### 3.3.3 Rotor System Drag Reduction

Tests were conducted using the candidate drag reduction devices, and a comparison was made with the reference, baseline case. This baseline case was tested without the sleeve fairings, the unmodified beanie and the unmodified pylon fairing. Drag force was computed and the corresponding  $C_{DS}$  figure calculated for whole system. Data are presented in table 2 for zero degrees targeted angle of attack. A negative  $\Delta C_{DS}$  represents a drag reduction compared to the baseline case. The blade sleeve fairing ‘1’ clearly offers drag reduction advantage compared to no sleeve fairing, and the modified beanie shape offers additional drag advantage.

## 4 CONCLUSIONS

A wind tunnel experiment to measure the individually resolved components of a helicopter model fuselage and rotor system drag has been described. The model design required a particular arrangement of load cells and load sensors, and the requirement to resolve both beanie and rotor forces independently led to the design of a concentric, co-axial system of rotating load cells. This led to particular signal processing issues, which in turn dictated the testing procedures, and these have been described in detail. Typical drag breakdowns have been presented, along with rotor system power and drag reduction, and advantageous configurations have been identified.

## Acknowledgements

The work was supported by the European Union Clean Sky Green Rotorcraft Research Programme under GRC-ITD Grant Agreement Number CSJU-GAM-GRC-2008-001 and Grant Agreement Number 267571.

## References

- <sup>1</sup> R.W. Prouty. *Helicopter Performance, Stability and Control*. PWS Engineering Publications, Boston, MA, USA, 1986.
- <sup>2</sup> D. Desvigne and D. Alfano. Rotor-head/ fuselage interactional effects on helicopter drag: influence of complexification of the rotor head geometry. *Paper 119, 39th European Rotorcraft Forum, Moscow, Russian Federation, 3rd - 6th September, 2013*.
- <sup>3</sup> Wayne Johnson. *Helicopter Theory*. Dover Publications, New York, USA, 1980.
- <sup>4</sup> J.G. Leishman. *Principles of Helicopter Aerodynamics*. Cambridge University Press, Cambridge, United Kingdom, 2nd edition edition, 2006.
- <sup>5</sup> P.F. Sheridan and R.P. Smith. Interactional aerodynamics - a new challenge to helicopter technology. *Journal of the American Helicopter Society*, 25(1):3–21, 1980.
- <sup>6</sup> P. Roesch and A-M Dequin. Experimental research on helicopter fuselage and rotor hub wake turbulence. *Journal of the American Helicopter Society*, 30(1):43–51, 1985.
- <sup>7</sup> R. Shenoy, M. Holmes, M.J. Smith, and N.M. Komerath. Computational investigation of hub drag deconstruction from model to full scale. *Paper 165, 37th European Rotorcraft Forum, Vergiate and Gallarate, Italy, 13th-15th September, 2011*.
- <sup>8</sup> A. LePape, C. Lienard, and J. Bailly. Active flow control for helicopters. *ONERA Aerospacelab Journal, Issue 6, June 2013, 2013*.
- <sup>9</sup> M. Potsdam and A. LePape. CFD investigations on a NACA 0036 airfoil with active flow control. *Paper AIAA-2008-3869, AIAA 4th Annual Flow Control Conference, Seattle, WA, 23rd-26th June, 2008*.
- <sup>10</sup> N.W. Schaeffler, B.G. Allan, C. Lienard, and A. LePape. Progress towards fuselage drag reduction via active flow control: a combined CFD and experimental effort. *Paper 064, 36th European Rotorcraft Forum, Paris, France, 7th-9th September, 2010*.

## Tables and Figures

Table 1: Summary of notional aerodynamic test conditions

Description	advance ratio $\mu$	rotor speed [RPM]	wind tunnel speed [ms <sup>-1</sup> ]	pitch range $\alpha$ [deg]	yaw range $\beta$ [deg]
Approach	0.183	664	20	0 to 14	0
Approach	0.183	664	20	10	-12 to 12
Cruise	0.365	748	45	-10 to 6	0
Cruise	0.365	664	40	-10 to 6	0

Table 2: Total  $C_D S$  change relative to baseline test configuration for rotating rotor, cruise case at targeted model incidence  $\alpha = 0^\circ$ . Data are ordered in terms of  $C_D S$  reduction, a negative figure is a drag reduction relative to the baseline. The reference configuration is indicated ‘ref’, and the modifications indicated as ‘1’ or ‘2’.

configuration	pylon fairing	blade sleeve fairing	beanie	$\Delta C_D S\%$
F0S1H1	ref	1	1	-6.6
F0S1H2	ref	1	2	-6.0
F0S1H0	ref	1	ref	-4.9
F1S1H1	1	1	1	-4.0
F0S0H1	ref	ref	1	-3.7
F0S2H2	ref	2	2	-3.4
F0S2H0	ref	2	ref	-2.2
F0S2H1	ref	2	1	-2.0
F0S0H2	ref	ref	2	-0.4
F1S2H1	1	2	1	0.8
F1S0H1	1	ref	1	1.1
F1S0H2	1	ref	2	5.6



Figure 1: CARD model in the wind tunnel. The rotor rotates clockwise, and the wind tunnel flow is from right to left. The beanie and rear engine pylon fairing have not been fitted, and the blade stubs and flexure sleeves can be seen. The access platform seen below the model is removed prior to testing.

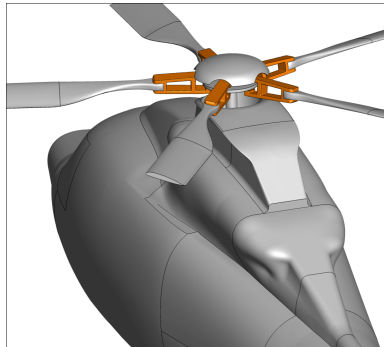


Figure 2: Baseline blade sleeve highlighted. Sleeve fairings cover the baseline sleeve only.

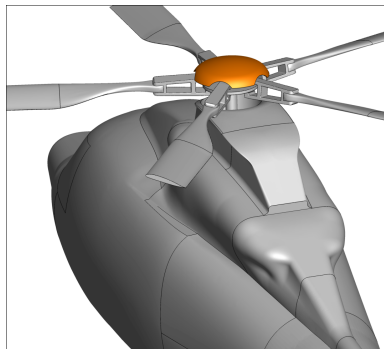


Figure 3: Baseline rotor beanie highlighted. Alternative beanies fitted had different geometry but the same diameter.

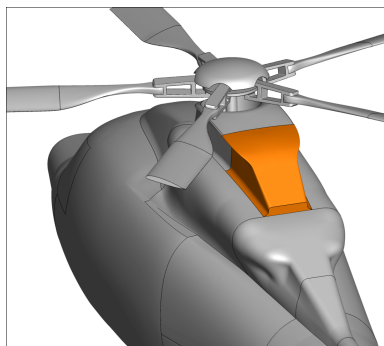


Figure 4: Baseline aft pylon fairing highlighted. The alternative pylon replaced the baseline pylon.



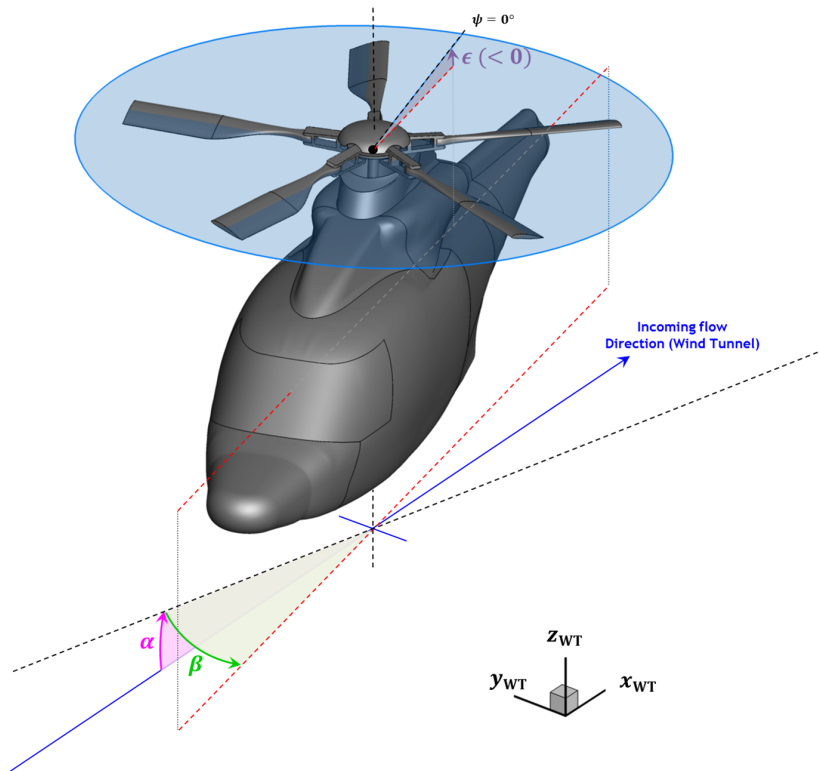


Figure 7: Model axis system showing model axis direction (dashed red line), wind tunnel flow direction, model angle of incidence  $\alpha$  and yaw angle  $\beta$ . The shaft tilt angle  $\epsilon$  is indicated.

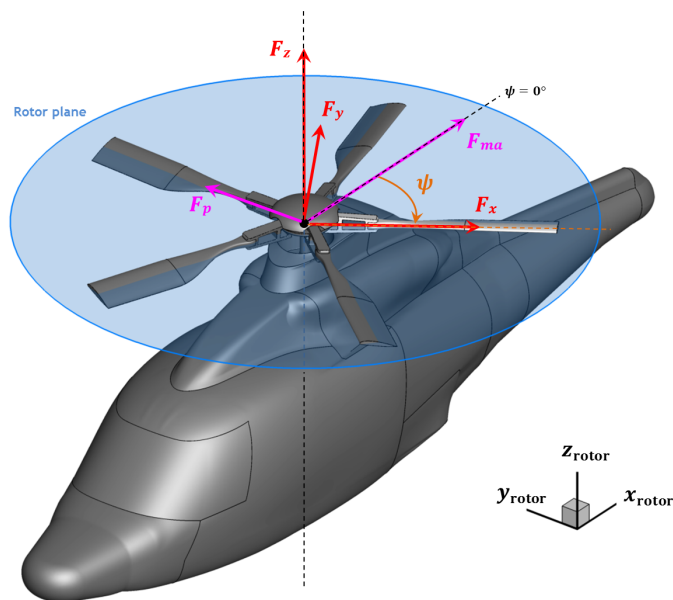


Figure 8: Rotor forces, load cell forces and rotor azimuth angle  $\psi$ . The force arrows are only intended to show directions and do not represent any proportional magnitudes. Load cell in-plane forces  $F_x$ ,  $F_y$  change orientation with rotor rotation about the rotor axis, and the forces  $F_{ma}$  and  $F_p$  are the rotor in-plane forces resolved into the fuselage axis and lateral directions respectively.

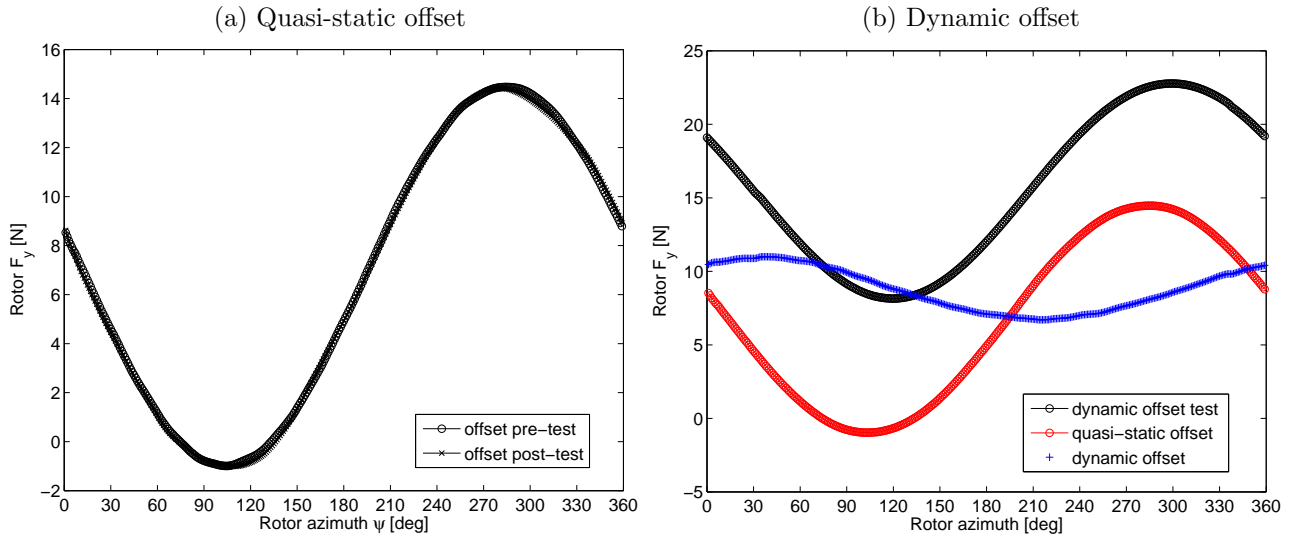


Figure 9: Quasi-static and dynamic offset for rotor typical  $F_y$  signal at zero model targeted pitch angle, force variation plotted as a function of rotor azimuth angle  $\psi$ . Frame (a) shows pre- and post- test quasi-static offset, data filtered at threshold  $10 \times$  rotor speed for quasi-static offset test. Frame (b) shows dynamic offset for the same configuration at rotor speed 744RPM, data are filtered at threshold  $2.5 \times$  rotor speed.

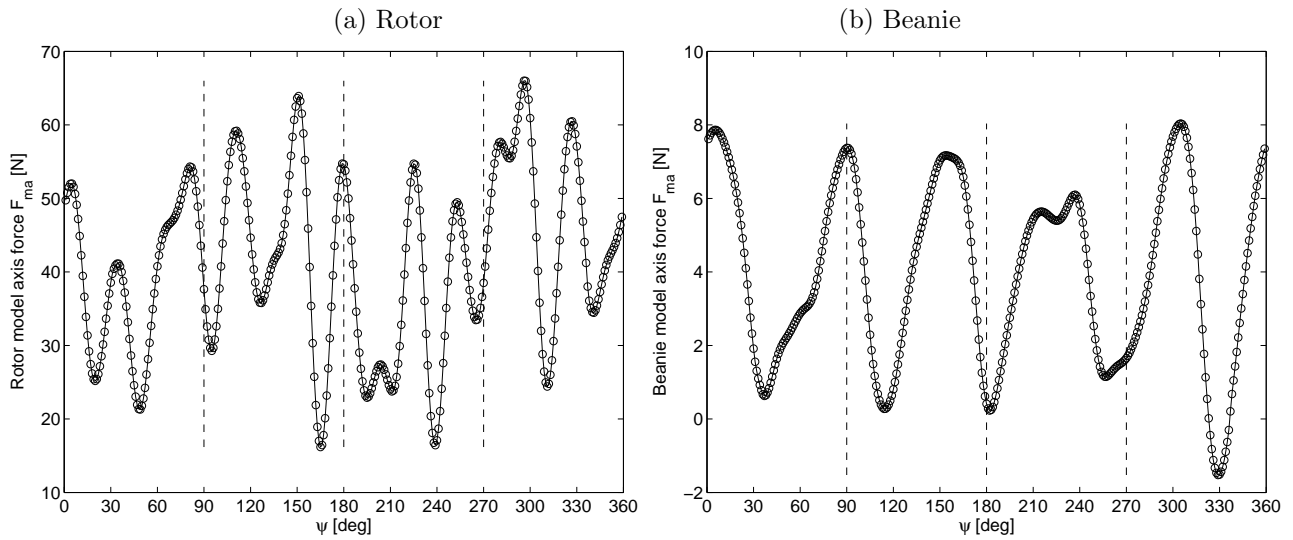


Figure 10: Rotor system in-plane force  $F_{ma}$  acting in direction of model axis, plotted as a function of rotor azimuth position. Frame (a) shows the contribution due to the rotor, frame (b) due to the beanie. Cruise configuration test at targeted model angle of incidence  $4^\circ$ , blade collective  $8^\circ$ , wind tunnel speed  $45\text{ms}^{-1}$ , rotor speed 744RPM.

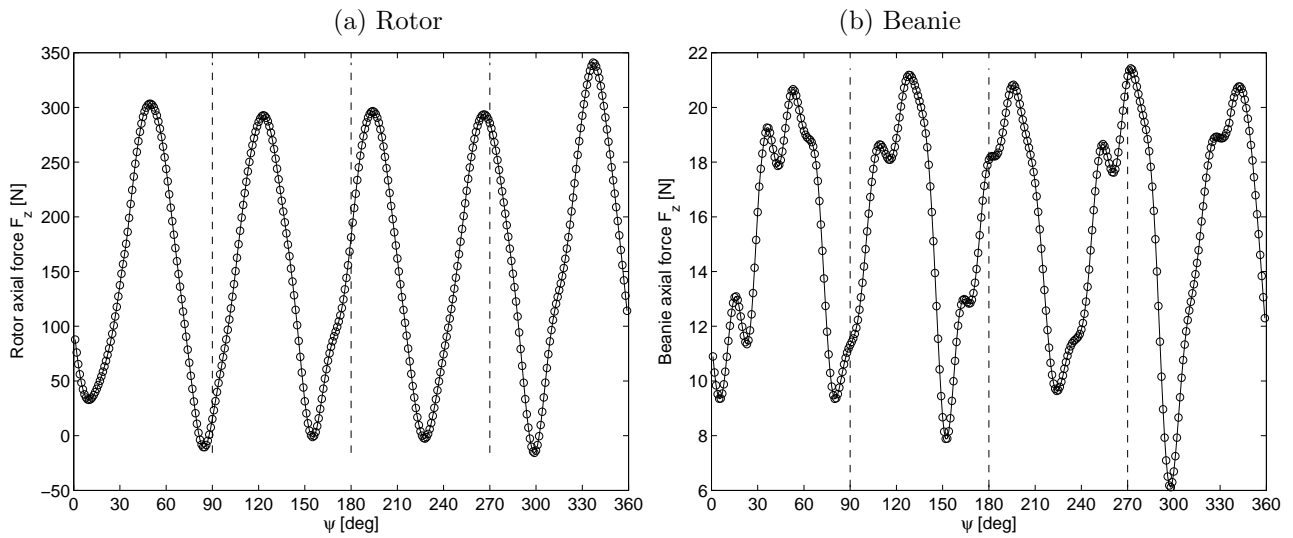


Figure 11: Rotor system axial force  $F_z$  plotted as a function of rotor azimuth position. Frame (a) shows the contribution due to the rotor, frame (b) due to the beanie. Cruise configuration test at targeted model angle of incidence  $4^\circ$ , blade collective  $8^\circ$ , wind tunnel speed  $45\text{ms}^{-1}$ , rotor speed 744RPM.

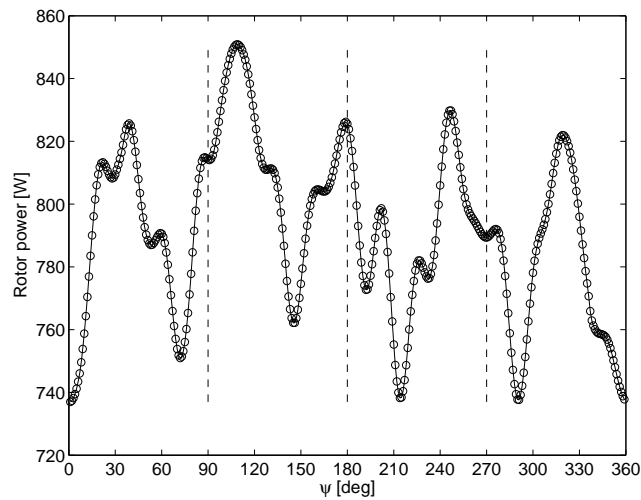


Figure 12: Rotor power plotted as a function of rotor azimuth position. Cruise configuration test at targeted model angle of incidence  $4^\circ$ , blade collective  $8^\circ$ , wind tunnel speed  $45\text{ms}^{-1}$ , rotor speed 744RPM.

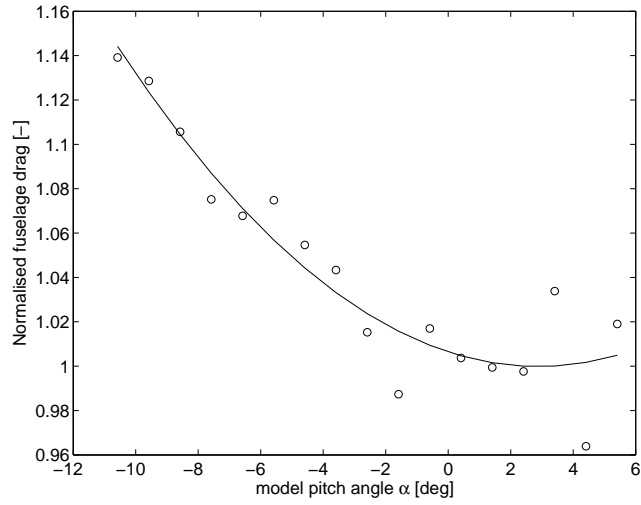


Figure 13: Fuselage drag plotted as a function of wind tunnel corrected model pitch angle. Drag is normalised by minimum curve fit fuselage drag for the configuration. Cruise configuration test, blade collective  $8^\circ$ , zero yaw angle, wind tunnel speed  $45\text{ms}^{-1}$ , rotor speed 744RPM. The solid line is a least squares quadratic fit to the data.

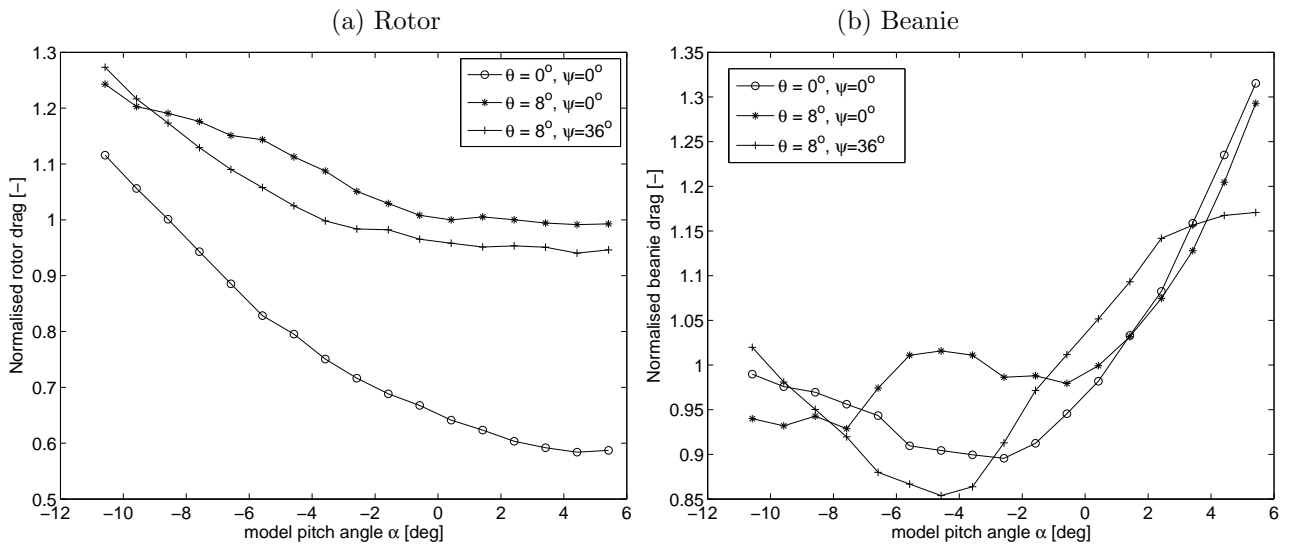


Figure 14: Normalised rotor and beanie drag plotted as a function of wind tunnel corrected model pitch angle for the non-rotating rotor. Plots for different rotor blade collective  $\theta$  and rotor fixed azimuth angle  $\psi$  are shown. Drag is normalised by the corresponding component drag value at  $\theta = 8^\circ$ ,  $\psi = 0^\circ$  at targeted incidence  $\alpha = 0^\circ$ . Cruise configuration test, zero yaw angle, wind tunnel speed  $45\text{ms}^{-1}$ , rotor speed 0RPM.

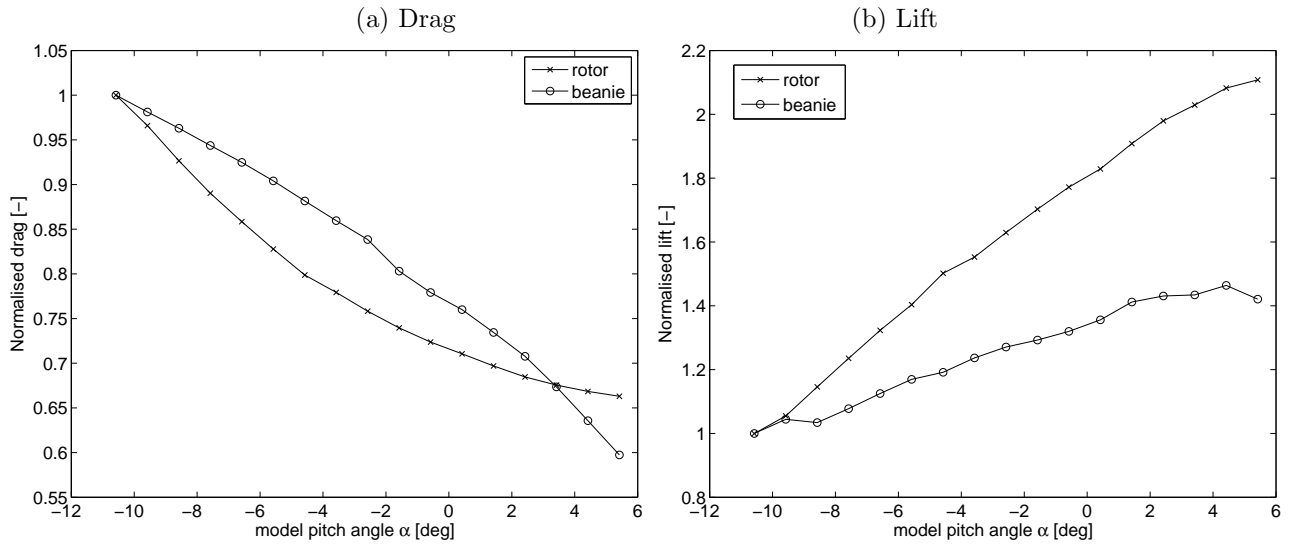


Figure 15: Normalised rotor and beanie lift drag for the rotating rotor plotted as a function of wind tunnel corrected model pitch angle. Drag and lift are normalised by the corresponding component values at targeted incidence  $\alpha = -10^\circ$ . Cruise configuration test, zero yaw angle, wind tunnel speed  $45\text{ms}^{-1}$ , rotor speed 744RPM. Rotor configuration identical to figure 13.

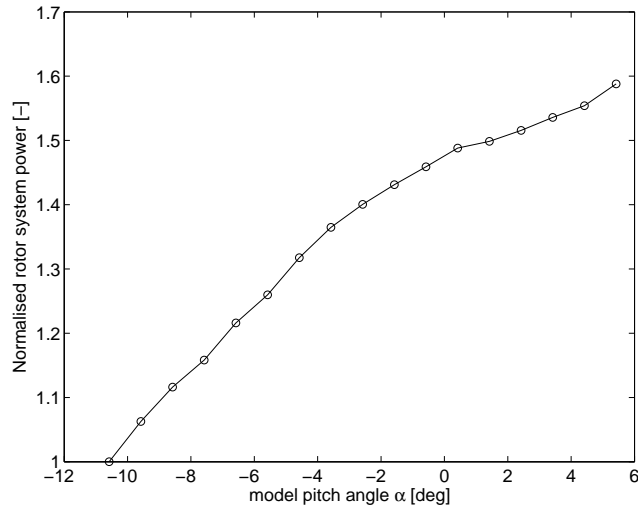


Figure 16: Normalised rotor system power for the rotating rotor plotted as a function of wind tunnel corrected model pitch angle. Power is normalised by the corresponding value at targeted incidence  $\alpha = -10^\circ$ . Cruise configuration test, zero yaw angle, wind tunnel speed  $45\text{ms}^{-1}$ , rotor speed 744RPM. Rotor configuration identical to figure 13.

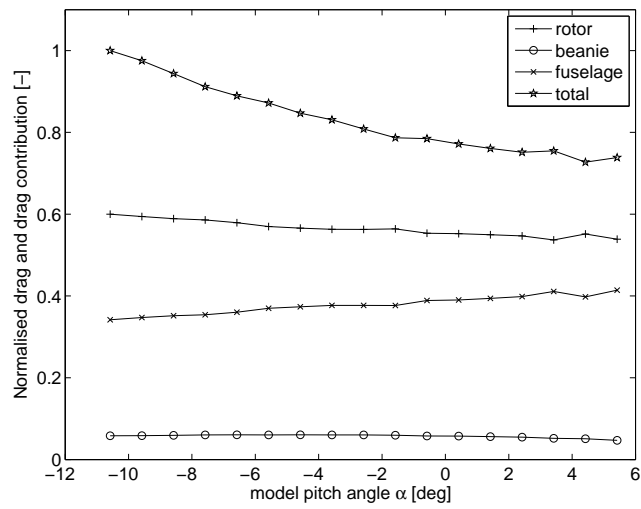


Figure 17: Component drag contribution to the total drag for rotor, beanie and fuselage, and normalised total drag, plotted as a function of wind tunnel corrected model pitch angle. Component contributions are relative to the total drag at the given  $\alpha$ , hence they add up to 1. Total drag plotted is normalised by the value at targeted incidence  $\alpha = -10^\circ$ . Cruise configuration test, zero yaw angle, wind tunnel speed  $45\text{ms}^{-1}$ , rotor speed 744RPM. Rotor configuration identical to figure 13.